Nature Communications

Article in Press

Co-upcycling spent lithium-ion batteries and plastics into microwave absorbing materials with Ni-Co catalyst control

Baolong Qiu, Yuanzhao Hou, Zhan Shi, Pin Du, Nuo Xu, Hongwei Xie, Kuiren Liu, Jianshe Chen, Binchuan Li, Qing Han, Dihua Wang, Lawrence Yoon Suk Lee, Mengjie Liu, Daxue Fu & Huayi Yin

We are providing an unedited version of this manuscript to give early access to its findings. Before final publication, the manuscript will undergo further editing. Please note there may be errors present which affect the content, and all legal disclaimers apply.

If this paper is publishing under a Transparent Peer Review model then Peer Review reports will publish with the final article.

Co-upcycling spent lithium-ion batteries and plastics into microwave absorbing materials with Ni-Co catalyst control

Baolong Qiu,[a,b,#] Yuanzhao Hou,[a,#] Zhan Shi,[c] Pin Du,[a] Nuo Xu,[a] Hongwei Xie,[a] Kuiren Liu,[a] Jianshe Chen,[a] Binchuan Li,[a] Qing Han,[a] Dihua Wang,[d] Lawrence Yoon Suk Lee,[b] Mengjie Liu,[e]* Daxue Fu,[a,]* Huayi Yin,[a,d,f,]*

[a] Key Laboratory for Ecological Metallurgy of Multimetallic Mineral of Ministry of Education, School of Metallurgy, Northeastern University, Shenyang, 110819, P. R. China.

[b] Department of Applied Biology and Chemical Technology and Research Institute for Smart Energy, The Hong Kong Polytechnic University, Hung Hom, Kowloon, Hong Kong SAR, China.

[c] Department of Land, Environment, Agriculture and Forestry, University of Padova, Legnaro (PD) 35020, Italy.

[d] School of Resource and Environmental Science, Wuhan University, Wuhan, 430072, P. R. China.

[e] Department of Chemistry, Northwestern University, Evanston, IL, 60202, USA.

[f] Key Laboratory of Data Analytics and Optimization for Smart Industry, Ministry of Education, Northeastern University, Shenyang, 110819, P. R. China.

[#] These authors contributed equally: Baolong Qiu, Yuanzhao Hou.

*Corresponding author, E-mails: Mengjie Liu mengjie.liu@northwestern.edu

Daxue Fu fudx@smm.neu.edu.cn;

Huayi Yin yinhuayi@whu.edu.cn;

Abstract

Co-upcycling plastics with lithium-ion batteries (LIBs) into carbon nanotubes (CNTs) offers a promising high-value approach; however, it is hindered by the challenge of poisoning metal catalysts by carbon deposition and the uncontrollable particle growth. Here, we propose a co-upcycling strategy to convert spent $LiNi_xCo_yMn_{1-x-y}O_2$ (NCM) and binary plastics—polyethylene terephthalate (PET) and other plastics—into $NiCoMnO_x$/CNTs composites (or materials) for microwave absorption. During the pyrolysis, the generated pyrolysis gas reduces the NCM to $NiCoMnO_x$ and Li_2CO_3, and the $NiCoMnO_x$ catalyzes the decomposition of pyrolysis gas to generate CNTs. Importantly, Li_2CO_3 suppresses the growth of NiCo particles to below 100 nm and PET as both an etching agent and a carbon source, achieving a carbon conversion rate of 33% while preventing $NiCoMnO_x$ poisoning. After heat treatment at 800 °C, the resulting material exhibits favorable microwave absorption with an effective absorption bandwidth (EAB, RL < −10 dB) of 7.01 GHz at 2.41 mm. Life cycle analysis (LCA) shows that this strategy has obvious environmental benefits. Overall, PET is a general enabler to prepare $(Ni_xCo_y)MnO$/CNTs microwave-absorbing materials harnessing carbon from binary plastics and critical metals from battery materials, providing a sustainable solution for upcycling spent LIBs and plastic wastes.

Keywords: spent lithium-ion batteries, plastic wastes, Li recovery, carbon nanotubes, electromagnetic wave absorption.

Introduction

Carbon neutrality is a key challenge for human society in achieving sustainable development goals.[1] The rapid growth of electric vehicles (EVs) has significantly increased the demand for lithium-ion batteries (LIBs), which are essential to achieving carbon neutrality.[2] Over the past decade, layered oxide ternary ($LiNi_xCo_yMn_{1-x-y}O_2$, NCM) batteries have dominated the market due to their high energy density and low temperatures performance.[3, 4] However, the lifespan of NCM batteries is typically limited to 5 to 8 years. Once their capacity decreases to 80%, they no longer meet the performance requirements of EVs.[5] Consequently, a large number of spent NCM batteries must be recycled to mitigate environmental, and health risks and prevent the depletion of critical metal resources, such as lithium, cobalt, and nickel.[6, 7] Therefore, it is crucial to develop green, energy-efficient, and economically viable recycling methods for NCM batteries.[8, 9] In contrast to traditional pyrometallurgical, hydrometallurgical, and direct regeneration approaches, converting spent LIBs into advanced functional materials offers a promising alternative.[10-12] Upgrading spent LIBs into catalysts for applications such as oxygen reduction reaction (ORR),[13, 14] oxygen evolution reaction (OER),[15, 16] hydrogen evolution reaction (HER),[17] and other functional materials has attracted increasing attention in recent years.[18-20] The concept of upcycling spent LIBs overcomes the limitations of traditional recycling, enhancing energy efficiency in waste processing while advancing the principles of the circular economy.

Plastic waste poses a serious environmental issue but also offers valuable recycling opportunities.[21, 22] Over 380 million tons are produced annually worldwide with most resisting degradation and harming ecosystems.[23] Incineration of plastic waste worsens carbon neutrality efforts by emitting CO_2 and toxic pollutants such as polycyclic aromatic hydrocarbons (PAHs), NO_x, and SO_x.[24] Pyrolysis technology offers a promising solution by converting plastic waste into pyrolysis gas,[25] fuel,[26] and valuable chemicals.[27] Notably, pyrolysis gas derived from waste plastics can serve as a carbon feedstock for the production of carbon nanotubes (CNTs) *via* chemical vapor deposition (CVD), particularly in the presence of metal catalysts such as Fe, Co,

and Ni.[28, 29] It has been shown that spent LIB cathode materials can function as catalytic centers for pyrolysis gas through the *in-situ* reduction of transition metals (TMs) during co-pyrolysis with organic wastes, such as biomass,[30] and plastic waste,[31] to produce carbon materials. Compared with H_2 and CO reduction,[32, 33] this reduction method has a relatively low reduction temperature while maintaining a high Li^+ leaching efficiency. However, the rapid release of volatiles during plastic pyrolysis may lead to TM catalyst deactivation due to high local gas concentrations, presenting a significant obstacle to the synthesis of TMs–CNT composites at low temperatures.[34-36] Thus, preventing catalyst deactivation and controlling the composition of TMs and CNTs in the composite materials are key goals to achieve the efficient utilization of spent NCMs and plastic waste.

This study investigates the deactivation of TMs during the co-pyrolysis of NCM cathode materials and plastics. By analyzing the deactivation mechanisms of TMs, we propose a mixed plastic pyrolysis process—specifically the "polyethylene terephthalate (PET) + plastic" co-pyrolysis. This process addresses the size limitation and catalyst deactivation issues of the spent NCM cathode and promotes an effective transformation to carbon nanotubes (CNTs). The inclusion of PET significantly inhibits the deactivation of TMs and enables the upcycling of spent NCMs into $(Ni_xCo_y)MnO/CNT$ composites. Microwave absorption measurements demonstrate that the resulting materials exhibit enhanced functional properties following a one-step thermal treatment. Additionally, environmental and economic analyses indicate that the co-pyrolysis process offers an effective method for safely treating plastic wastes while simultaneously recycling and upgrading spent NCM batteries.

Results

Fig. 1a shows the internal design of the primary reactor, with a stainless steel mesh in the middle, a waste plastic polyethylene (PE), and polyethylene terephthalate (PET) processing chamber at the bottom, and a spent $LiNi_xCo_yMn_{1-x-y}O_2$ (NCM) cathode material processing chamber at the top. This configuration allows for the production and separation of Li_2CO_3 and transition metals (TM) such as Co, Mn, and Ni. Water leaching can selectively extract Li_2CO_3 from the pyrolysis product $(Ni_xCo_y)MnO/CNT-Li_2CO_3$. Following a one-step heat treatment, $(Ni_xCo_y)MnO/CNT$ can be further upgraded to a microwave-absorbing material.

Fig. 1b shows Ellingham diagrams for $LiNi_{0.8}Co_{0.1}Mn_{0.1}O_2$ (NCM811) were calculated in the presence of potential pyrolysis gas components at 1 mol standard state, the NCM811 can be reduced to Ni, Co, and MnO at the plastic pyrolysis temperature of 450-550 °C. SEM images (**Fig. 1c**) show that after 3 wt% PET was added (NCM811/PE/PET mass ratio = 1/30/1), the product changes from a carbon-coated structure of about 10-15 μm to a cross-carbon nanotube structure, indicating that PET inhibits the deactivation of TM active sites and grows into carbon nanotubes (CNTs). High-angle annular dark field (HAADF) scanning TEM and EDX elemental mapping images also confirmed the deactivation of NiCo alloy without PET addition (**Fig. S2**). The formation process of $(Ni_xCo_y)MnO/CNTs$ can be divided into three stages (**Fig. S3**). First, the Li–O–TM layered structure of NCM acts as a template for Li_2CO_3 formation during delithiation, maintaining the nanoscale morphology of the transition metal framework and inhibiting particle growth. Second, NiCo alloy and MnO nanoparticles (~40–100 nm) form on the surface through phase separation and particle refinement. Finally, carbon-containing gas is adsorbed on the nanoscale NiCo particles, promoting CNT nucleation and growth in a manner similar to conventional CVD processes. The synergistic effect of the Li_2CO_3 template and Ni-Co catalyst size control ultimately generates $(Ni_xCo_y)MnO/CNTs$. **Fig. 1d** shows the powder XRD (PXRD) patterns of the products with increasing amounts of PET feeding, showing an enhanced carbon peak 25.9° (002) assigned to CNTs, while the metal peaks at 44.5°,51.6°, and 75.9°correspond to

the NiCo alloy. Notably, when the mass ratio of NCM811/PE/PET is 1/30/1 the reaction temperature is 550 °C, and the reaction time is 5 h, the optimal Li^+ leaching efficiency reaches 99.9% (**Fig. 1e**). The continuous reaction interfaces between gas and solid phases can effectively accelerate the reaction process and improve the Li^+ extraction efficiency. However, when only PE was engaged without PET, the embedded LTMO remained unreacted, beneath the deactivated metal layer by carbon accumulation, leading to a low Li extraction efficiency of 81.4% (**Fig. S4**). Through the fine-tuning of the reactant mass ratio, the pyrolysis behaviors of the NCM811/PE/PET systems are summarized (**Figs. S5 to S7**).

Fig. 1f shows the mechanism. When LTMOs are co-pyrolyzed with pure PE plastics, the rapidly released plastic pyrolysis gases usually catalyze dehydrogenation and form carbon atoms on the reduced TM surface. When the adsorption rate of carbon atoms on TM is greater than its release rate, it results in the over-deposition of carbon and deactivation of the TM active sites. In this study, CO/CO_2 released by PET pyrolysis is introduced to achieve dehydrogenation by reacting with plastic pyrolysis gases such as ethylene, acetylene, benzene, etc., thereby preventing the deactivation of metal catalytic sites (**Fig. S8**). Mass spectrometry analysis clearly shows the CO and CO_2 signals during the co-pyrolysis of PET and plastic. PE/PP mainly generates C_1–C_4 hydrocarbons, creating a strongly reducing and oxygen-deficient atmosphere. PS produces aromatic-rich vapors (e.g., styrene, ethylbenzene), promoting carbon deposition and increasing coking tendency. PC produces a higher concentration of CO_2, thus creating a strongly oxidizing atmosphere. Quantitative analysis of the gas phase composition using GC curves showed that, in the presence of NCM, the final gas phase products transformed from the characteristic products of single plastic pyrolysis to CH_4 (80-90%), H_2 (7-8%), and a small amount of CO_2 (0.5%). The main components of PET pyrolysis gas are CO (22.8%) and CO_2 (8.33%) as well as the Gibbs free energy of deoxygenation reaction (**Text S1 and Figs. S9 to S10**). As shown in **Fig. 1g**, the gas isotherms at different pressures were calculated by HSC 6.0, proving that there is a disproportionation reaction of CO at 550 °C, 1 Mpa. When 3 wt% PET is added, the weight loss

before 400 °C is reduced to 0.6%, which means that PET as an etchant significantly inhibits the formation of amorphous carbon and improves the purity of CNTs (**Fig. S11**). Therefore, the above results prove that the addition of PET to co-pyrolysis can achieve in-situ cleaning of amorphous carbon, higher Li^+ leaching efficiency, and carbon conversion rate.
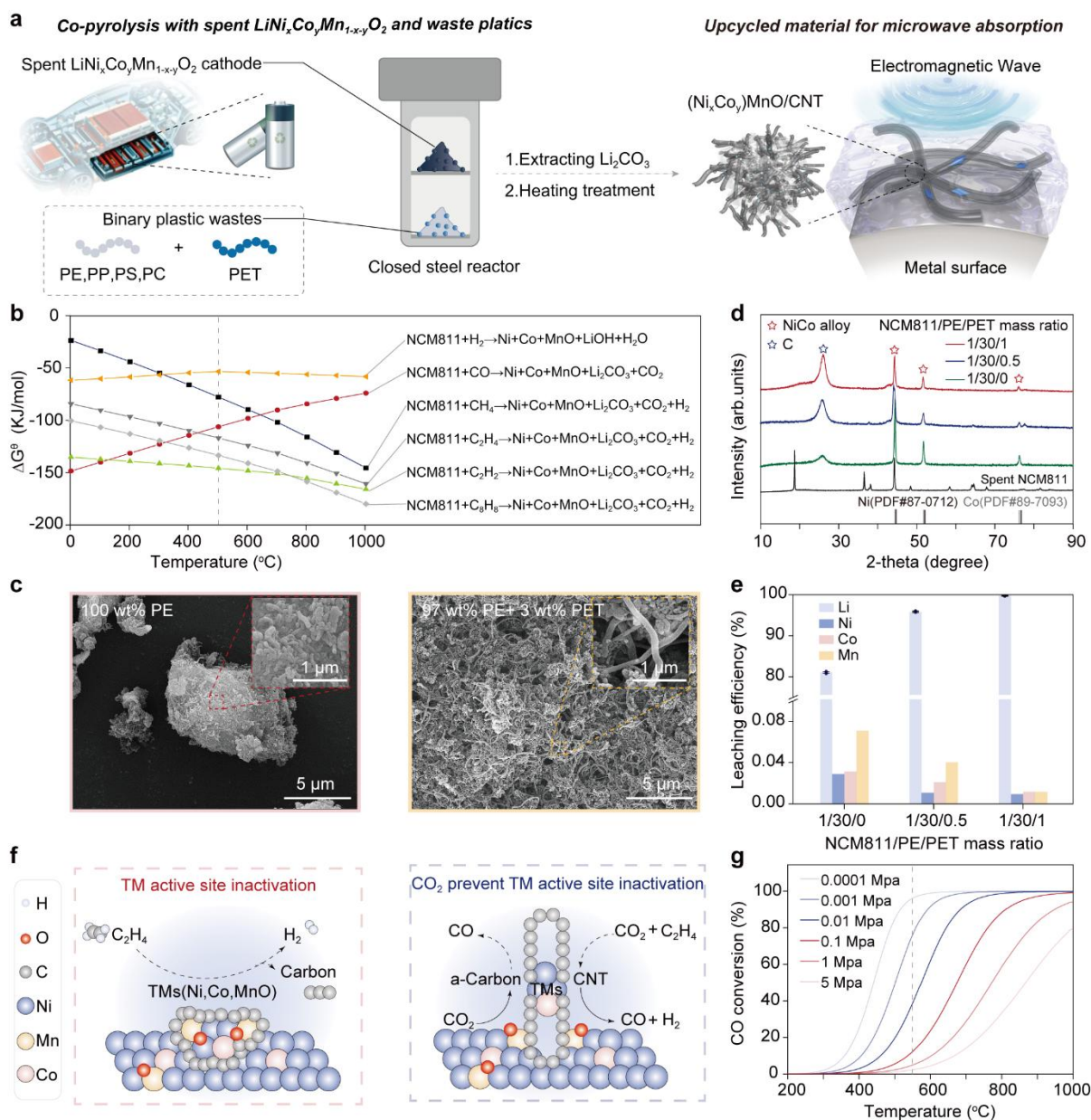

Fig. 1. Co-upcycling spent NCM cathodes and binary plastics. a, Conceptual design of the co-pyrolysis process of spent NCM cathodes and binary plastic wastes; **b,** Elling diagrams illustrating NCM with

different pyrolysis gases; **c,** SEM images of 0 wt% PET added and 3 wt% PET added; **d,** PXRD patterns of NCM811 products; **e,** Li, Ni, Co, and, Mn leaching efficiency under different NCM811/PE/PET mass ratios (550 °C, 5 h); **f,** Regulating mechanism of PET pyrolysis gas on the growth of NiCo alloy/CNTs; **g,** Relationship between the established gas composition and temperature for the gasification of carbon. Error bars indicate the standard deviation of three independent measurements. Representative SEM images are shown; the experiments were independently repeated three times with similar results.

Microwave absorbing materials with excellent performance can be obtained by heat treatment process and adjusting TMs/CNT ratio. In this study, the product obtained after co-pyrolysis at 550 °C for 5 h is named $(Ni_8Co_1)MnO/CNT$. The product processed by calcination at 800 °C for 1 h in Ar atmosphere is named $(Ni_8Co_1)MnO/CNT-800$; the product using NCM622 instead of NCM811 under the same reaction conditions is named $(Ni_6Co_2)MnO/CNT-800$. **Fig. 2a** is the XRD spectrum of the final product after calcination, which shows that the alloy crystallinity of $(Ni_8Co_1)MnO/CNT-800$ is stronger than that of $(Ni_6Co_2)MnO/CNT-800$, and the splitting and shifting of small alloy peaks occur. The Raman spectrum of **Fig. 2b** shows that $(Ni_8Co_1)MnO/CNT-800$ exhibits a *D*-to-*G* peak intensity ratio (1.27). More interestingly, the harmonic peaks of *D* peek and *G* peek appear in the range of 2250-3500 cm^{-1} and have multiple split peaks. This is mainly due to the wide-diameter distribution of multi-walled CNTs and more defects.

Fig. 2c shows the SEM image of $(Ni_8Co_1)MnO/CNT-800$, where the CNTs appear bent and entangled, exhibiting a board distribution in both diameter and length. High-angle annular dark-field (HAADF) scanning TEM and EDX elemental mapping images confirm that the catalyst is encapsulated within the CNTs (**Fig. 2d**). The even distribution of Ni and Co, without detectable Mn signal, suggests the successful separation of metal species in NCM811. The high-resolution TEM image **(Fig. 2e)** reveals the NiCo particles anchored at the middle of the CNT, indicating the catalytic role of the alloy in the epitaxial growth of CNTs. The corresponding inverse Fourier transformed (FT) images are indexed to the (111) lattice planes in hexagonal NiCo alloy, with fringe spacings of 2.01 Å. **Fig. 2f** presents the SEM image of $(Ni_6Co_2)MnO/CNT-800$ with a "sea urchin-like" morphology and a shorter CNT length. HAADF scanning TEM images show CNTs with diameters of about 80-100 nm, thick tube walls, and short lengths. EDX elemental mapping images also confirm the Mn separation from NCM622 and the formation of NiCo alloy. The high-resolution TEM image (**Fig. 2h**) shows that the NiCo particles are anchored at the end of the CNTs,

with the inverse FT image indexed to the (200) lattice plane of the hexagonal NiCo alloy, with a fringe spacing of 1.73 Å.

Fourier transform infrared spectroscopy (FTIR) and X-ray photoelectron spectroscopy (XPS) confirmed that the amorphous carbon of CNTs was removed after heat treatment. The FTIR spectrum in **Fig. 2i** shows peaks at 3438 cm^{-1} (O–H), 1170 cm^{-1} (C–O), 1380 cm^{-1} (–CH$_3$), and 1630 cm^{-1} (C=C). The chemical states of the elements present on the (Ni$_8$Co$_1$)MnO/CNT, (Ni$_8$Co$_1$)MnO/CNT-800, and (Ni$_6$Co$_2$)MnO/CNT-800 surface were investigated using full scan XPS (**Figs. S12 and S13**). The C 1s spectrum (**Fig. 2j**) can be decomposed into five bands: carbon in graphite (284.5 eV), defects caused by missing carbon atoms (285.4 eV), C-O species (286.1 eV), carbon bound to two oxygens (*i.e.*, –COOH, 288.7 eV), and the characteristic vibration lines of carbon in aromatic compounds (π–π* transition, 290.5 eV). The peaks in question can be divided into sp^3-C (284.4 eV), sp^2-C (284.0 eV), and sp^1-C (283.5 eV), corresponding to C−C, C=C, and C≡C, respectively. The peak area of (Ni$_8$Co$_1$)MnO/CNT-800 sp^2-C increases after heat treatment, which corresponds to the enhancement of the C=C peak in FTIR. Subsequently, we evaluated the electrical conductivity (σ) of the powder specimens under 30 MPa pressure, as depicted in **Fig. 2k**. The average conductivity is from high to low (Ni$_8$Co$_1$)MnO/CNT-800 (11.28 S/cm)> (Ni$_6$Co$_2$)MnO/CNT-800 (8.31 S/cm)>(Ni$_8$Co$_1$)MnO/CNT (3.30 S/cm). The average resistivity is from low to high (Ni$_8$Co$_1$)MnO/CNT-800 (0.09 Ω·m)< (Ni$_6$Co$_2$)MnO/CNT-800 (0.12 Ω·m)< (Ni$_8$Co$_1$)MnO/CNT (0.30 Ω·m). The above results show that heat treatment can remove surface amorphous carbon and reduce the defects of carbon nanotubes, thereby improving conductivity; a decrease in the alloy ratio Ni: Co will increase the diameter of carbon nanotubes and shorten their length.
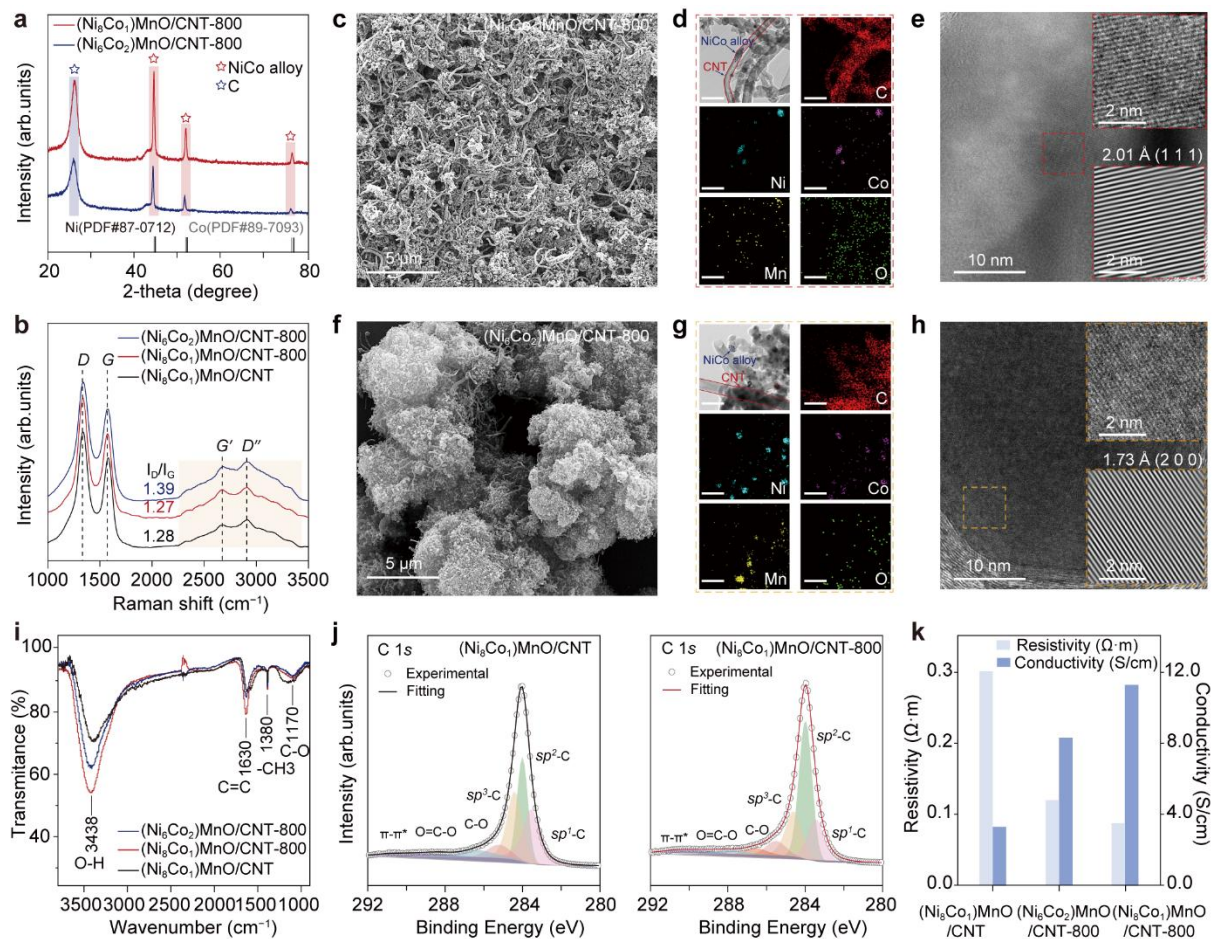
Fig. 2. Structural and morphological characterization of (Ni$_x$Co$_y$)MnO/CNT. a, PXRD patterns of (Ni$_8$Co$_1$)MnO/CNT-800 and (Ni$_6$Co$_2$)MnO/CNT-800; **b,** Raman shift of (Ni$_8$Co$_1$)MnO/CNT-800, (Ni$_6$Co$_2$)MnO/CNT-800, and, (Ni$_8$Co$_1$)MnO/CNT; SEM images of **c,** (Ni$_8$Co$_1$)MnO/CNT-800 and **f,** (Ni$_6$Co$_2$)MnO/CNT-800, HAADF-STEM image and the corresponding EDX mapping images of **d** and **g**; scale bar is 500 nm. High-resolution TEM image of **e** and **h**. The lattice planes of the NiCo alloy are shown in the figure; **i,** FTIR of (Ni$_8$Co$_1$)MnO/CNT-800, (Ni$_6$Co$_2$)MnO/CNT-800, and, (Ni$_8$Co$_1$)MnO/CNT, **j,** C 1s spectra of (Ni$_8$Co$_1$)MnO/CNT-800 and (Ni$_8$Co$_1$)MnO/CNT; **k,** Resistivity and conductivity of (Ni$_8$Co$_1$)MnO/CNT-800, (Ni$_6$Co$_2$)MnO/CNT-800, and, (Ni$_8$Co$_1$)MnO/CNT. Representative SEM images are shown; the experiments were independently repeated three times with similar results.

Based on the generalized transmission line theory, we have systematically evaluated the electromagnetic wave absorption (EMWA) performance of $(Ni_xCo_y)MnO/CNTs$, adhering to the methodology outlined in **Eqs. 9 to 11**.[37] Conventionally, the lower RL value signifies superior EMWA performance, with the RL threshold of −10 dB indicative of 90% absorption of the incident electromagnetic wave. **Fig. 3a** shows that the mass ratio of alloy to CNT in $(Ni_8Co_1)MnO/CNT$ and the heat treatment temperature can significantly adjust the dielectric constant of the material, thereby affecting the microwave absorption performance. The detailed dielectric constant and 2D diagrams of RL value (**Figs. S14 and S15**). **Figs. 3, b and d** show the 2D diagrams of RL value, it can be seen that the $(Ni_8Co_1)MnO/CNT$-800 after heat treatment has the widest absorption band at a thickness of 2.41 mm, and the EAB is 7.01 GHz, while the $(Ni_8Co_1)MnO/CNT$ before heat treatment cannot achieve effective absorption of electromagnetic waves in the range of 2−18GHz. This shows that heat treatment has a key influence on the wave absorption performance of $(Ni_8Co_1)MnO/CNT$, which is also reflected by the dielectric constant (**Fig. S16**). The VSM static magnetic measurement curves are provided in the **Fig. S17**, and the corresponding magnetic data, including saturation magnetization and coercivity, are summarized in the **Table. S1**. In addition, the adjustment of the alloy ratio also affects the wave absorption performance. The widest EAB of $(Ni_6Co_2)MnO/CNT$-800 at 2.26 mm is 5.22 GHz. The 3D diagrams of RL value (**Fig. S18**). Waveguide method verification curve and detailed sample test data are shown in **Figs. S19-31**, **Table S2**. To clarify the basis of the excellent EMWA performance of the sample, we conducted an in-depth analysis and carefully explored its impedance matching characteristics in combination with the normalized impedance Z. Obviously, the RL 2D diagram has a distribution law consistent with the |Z-1| two-dimensional model (**Figs. 3, e to g**). Taking the $(Ni_8Co_1)MnO/CNT$-800 sample as an example, when the coating thickness is 1.90 mm, RL_{min} reaches −59.19 dB, while |Z-1| reaches the lowest point of 0.0022. This correlation shows that the reduction of |Z-1| value is closely related to the reduction of RL value, emphasizing that the recovery of EMWA loss by MAM originates not only from the attenuation constant α, but also from the optimized impedance

matching. By analyzing the 1/4 λ curves of all samples (**Fig. S32**), a repetitive pattern emerges: RL$_{min}$ usually behaves as an odd multiple of the 1/4 λ point. In addition, as the matching thickness increases, the RL value shifts to lower frequencies, seamlessly aligning with the quarter-wavelength theoretical model.[38]

Fig. 3i shows the attenuation constant curve of the sample at 2−18 GHz. The larger the attenuation constant, the stronger the electromagnetic loss capability in the circuit. The loss in the medium is reflected in the form of heat energy. The attenuation constant of (Ni$_x$Co$_y$)MnO/CNTs shows regularity, and (Ni$_8$Co$_1$)MnO/CNT-800> (Ni$_6$Co$_2$)MnO/CNT-800> (Ni$_8$Co$_1$)MnO/CNT indicates that (Ni$_8$Co$_1$)MnO/CNT-800 has the strongest electromagnetic loss capability. To discern the dielectric loss mechanisms, we decomposed it into polarization loss. ε_p'' and conduction loss ε_c''. Based on the parallel/series resistance-capacitance circuit model (**Eq. 6**), supplemented by a nonlinear least-squares fitting approach.[39] It is worth noting that the proportion of ε_p'' in (Ni$_8$Co$_1$)MnO/CNT-800 is reduced, which is attributed to the enhancement of conduction loss (**Fig. 3h**). **Fig. 3j** further illustrates the relationship between ε_p'' and ε_c'' in 2−18 GHz. Among them, (Ni$_8$Co$_1$)MnO/CNT-800 exhibit a synergistic effect of polarization loss and conduction loss ($1 \leqslant \varepsilon_p''/\varepsilon_c'' \leqslant 10$) in the full spectrum range (2−18 GHz), while (Ni$_8$Co$_1$)MnO/CNT-500 exhibits a polarization loss-dominant effect ($\varepsilon_p''/\varepsilon_c'' \geqslant 10$). (Ni$_6Co_2$)MnO/CNT-800 exhibit a synergistic effect of polarization loss and conduction loss in the range of 2−12 GHz, while polarization loss dominates in the high-frequency range (12−18 GHz), which means that heat treatment and adjustment of alloy ratio have a key influence on dielectric loss.

In addition, Cole-Cole semicircles are used to validate each polarization relaxation process according to the Debye theory and **Eq. 7**.[40] The thermal treatment temperature and the added amount of carbon source (PE) systematically manipulated the evolution of the dielectric loss mechanism from polarization relaxation to conductivity loss. After thermal treatment, the Cole-Cole plots of all samples (**Figs. S33 to 36**) showed a decrease in both the number and diameter of semicircles, indicating a shorter polarization time and reduced relaxation processes. Notably, all

samples treated between 500 °C and 900 °C exhibited an elongated tail, indicating that conductivity loss became increasingly significant due to the strong conductive network formed by carbon nanotubes (CNTs). The multiple Debye relaxation was attributed to the $(Ni_xCo_y)MnO/CNT$ heterogeneous and numerous defects. We systematically compared the performance of our best samples with that of state-of-the-art NiCo/CNT-based and NiCo/dielectric composite absorbers reported in recent literature, using comprehensive comparative tables and visualizations. The results demonstrate that the $(Ni_8Co_1)MnO/CNT$-800 achieves an excellent balance between key performance metrics, including minimum thickness, low filler content, broad bandwidth, and high absorptivity, confirming its superior overall performance. Detailed data and visualizations are provided in the corresponding **Fig. S37** and **Table S3**.
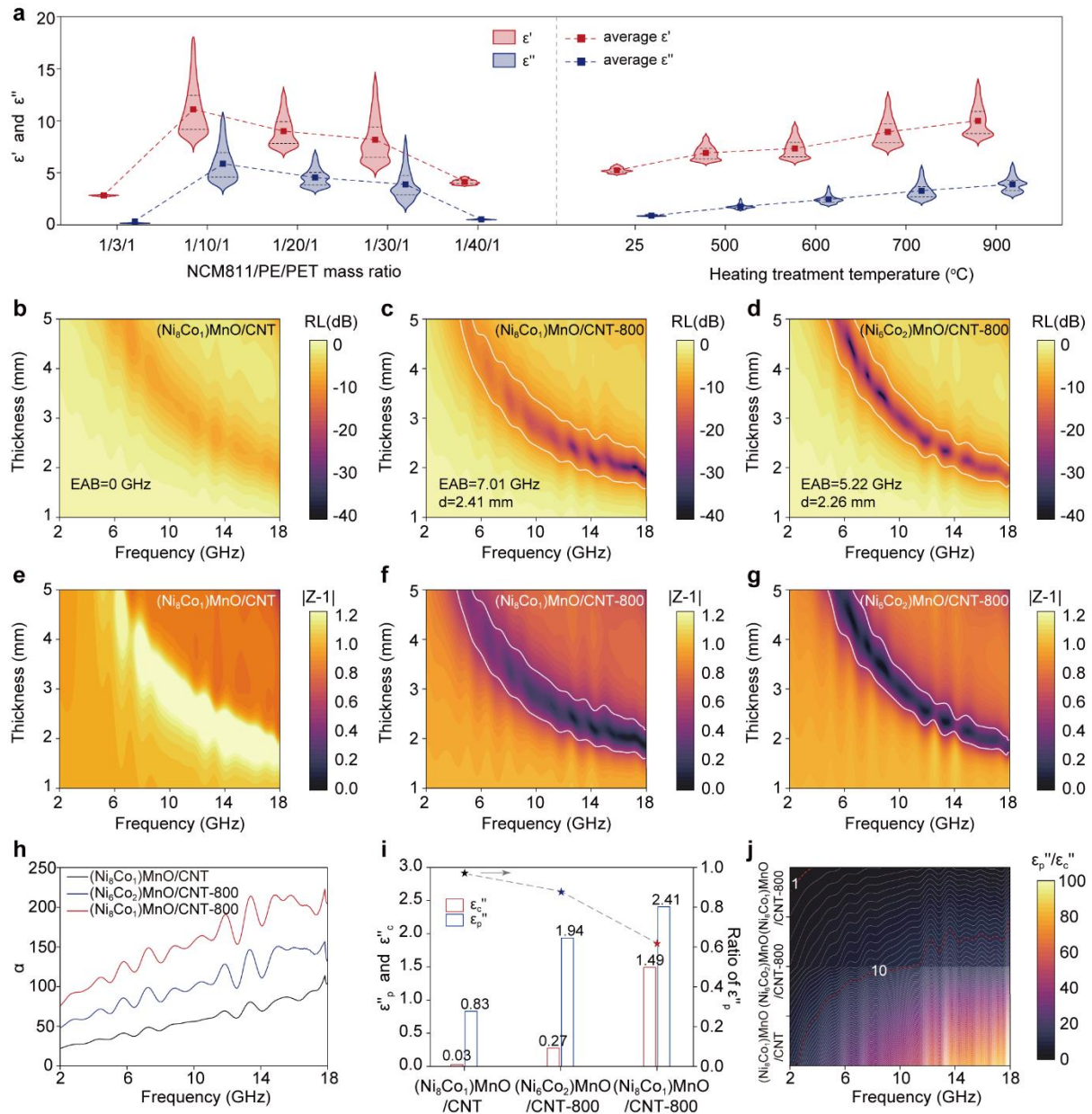
Fig. 3. Effect of preparation conditions of $(Ni_xCo_y)MnO/CNT$ on microwave absorption performance.
a, Violin plots of the real (ε', red) and imaginary (ε'', blue) parts of the complex permittivity as a function of the NCM811/PE/PET mass ratio (left) and heating temperature (right). The central line indicates the mean value, and the inner lines represent the first and third quartiles (25th and 75th percentiles). Squares connected by dashed lines show the average values. Data were obtained from $n = 3$ independent measurements. Complex permittivity; EMWA performance of $(Ni_8Co_1)MnO/CNT$, $(Ni_8Co_1)MnO/CNT$-800, and, (Ni_6Co_2) MnO/CNT-800, **b, c,** and **d,** 2D RL values, **e, f,** and **g,** impedance matching for $|Z-1|$, **h,** attenuation constant, **i,** polarization loss ε_p'' and conduction loss ε_c'' and **j,** corresponding $\varepsilon_p''/\varepsilon_c''$.

Fig. 4a shows the microwave absorption mechanism of $(Ni_xCo_y)MnO/CNT$, where the energy is converted from electromagnetic energy to electrical energy and finally dissipated in the form of thermal energy. The energy loss mechanism is mainly composed of dipole polarization loss, interface polarization loss, and conductive loss.[41] The radar cross section (RCS) serves as a pivotal metric for evaluating the actual far-field EMWA performance of reactive materials in their operational environment, which can assess the material's military significance and constitute a crucial aspect of radar stealth technology.[42, 43] To gain deeper insights into the EMWA stealth function of the samples as MAMs, we conducted simulations of the RCS distribution for the perfect electric conductor (PEC) flat plate (200 mm × 200 mm × 2.41 mm) and the PEC flat plate coated with the samples in realistic application scenarios based on the far-field response using a frequency domain solver. The simulation model consists of $(Ni_xCo_y)MnO/CNT$ and a PEC. The reflection signal intensity of the pure PEC plane and the $(Ni_xCo_y)MnO/CNT$ coating under the vertical incident electromagnetic wave is monitored at the entire detection angle (**Fig. 4b**). The PEC plate yields the maximum RCS of 18.70 dB m², whereas the PEC covered by $(Ni_8Co_1)MnO/CNT-800$ is −16.35 dB m², which means that it minimizes radar reflections by up to −35.05 dB m² at 2.41 mm. As shown in **Fig. 4c**, the 3D RCS distribution of $(NiCo)MnO/CNT$ presents different shapes, the vertical reflection intensity of $(Ni_8Co_1)MnO/CNT-800$ is much weaker than that of $(Ni_6Co_2)MnO/CNT-800$ and $(Ni_8Co_1)MnO/CNT-550$, indicating that $(Ni_8Co_1)MnO/CNT-800$ can achieve perfect absorption of electromagnetic waves.

To evaluate the photothermal conversion capability and environmental adaptability of the $(Ni_xCo_y)MnO/CNT$ heterostructure, the heat dissipation capacity of the $(Ni_8Co_1)MnO/CNT-800$ sample under an ultraviolet (UV) light source was observed using infrared thermal imaging technology.[44] $(Ni_8Co_1)MnO/CNT-800$ exhibits excellent thermal conductivity (**Fig. 4d**). At the UV light, the temperature of the composite material increased from room temperature to 100 °C within 10 s and maintained at 100 °C for 300 s. Subsequently, as the UV light was turned off, the temperature dropped synchronously from 100 °C to 38.6 °C in only 9 s (**Fig. 4e**). The results show

that $(Ni_8Co_1)MnO/CNT-800$ materials can convert photovoltaic energy into thermal energy and dissipate it in time through the synergistic effect of dielectric polarization (interface polarization and dipole polarization) and eddy current loss.
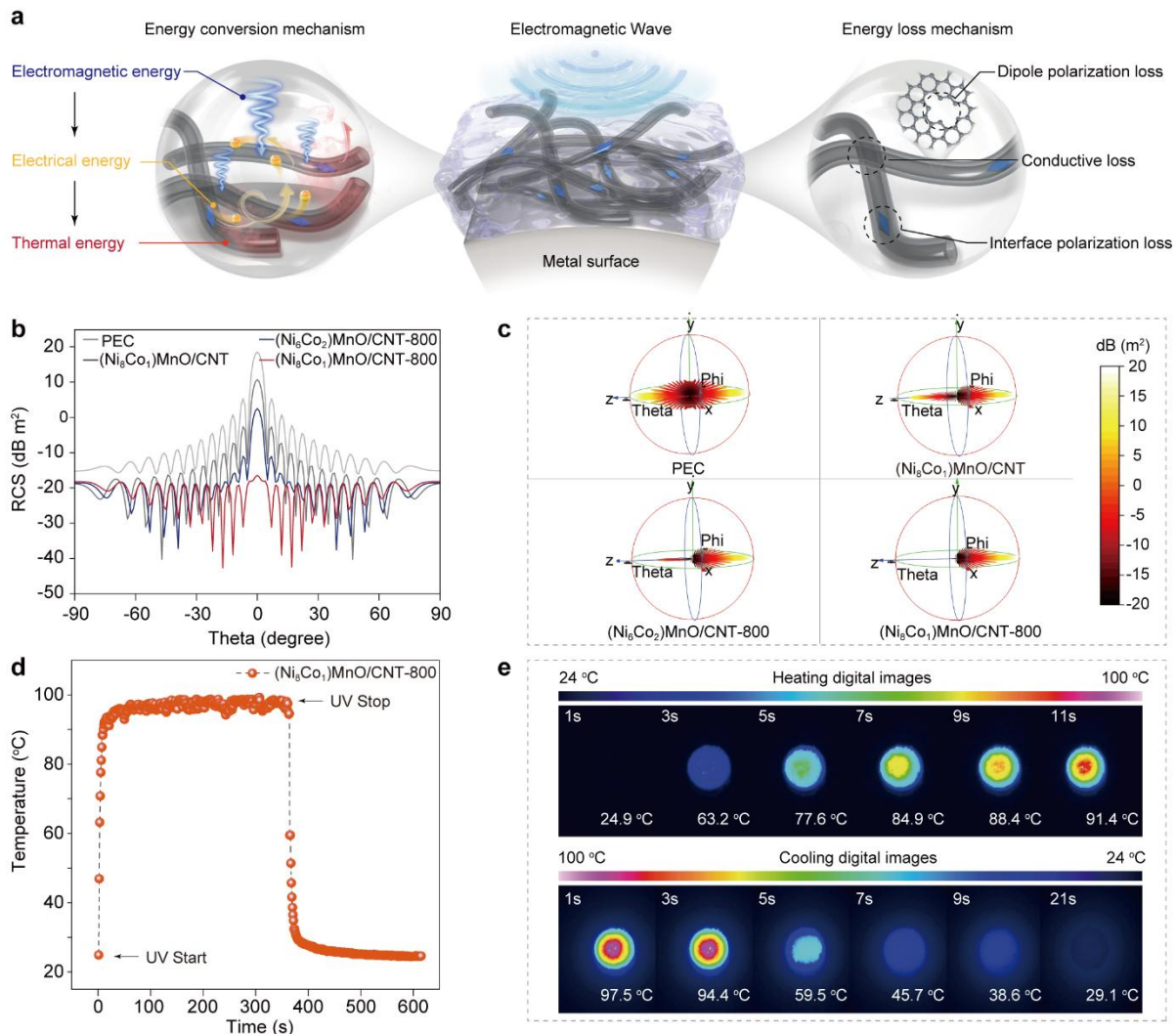
Fig. 4. Schematic diagram of electromagnetic wave absorption and heat dissipation performance of $(Ni_xCo_y)MnO/CNT$. a, Wave absorption mechanism diagram; **b,** RCS simulation curves and **c,** 3D RCS signals of PEC substrate covered with $(Ni_8Co_1)MnO/CNT$, $(Ni_6Co_2)MnO/CNT-800$, and, $(Ni_8Co_1)MnO/CNT-800$; **d,** Heating and cooling curves of $(Ni_8Co_1)MnO/CNT-800$ and **e,** corresponding digital images.

The binary plastic pyrolysis process with PET as an etching agent shows promising industrial prospects. To further evaluate its applicability, we conducted co-pyrolysis of four commonly used engineering plastics (LDPE, PP, PC, PS) with PET and NCM cathodes (NCM811, NCM622). **Fig. 5a** shows the XRD patterns of the products NiCo alloy and carbon peaks. The (111) diffraction peak of the NiCo alloy exhibits a slight shift under different plastic pyrolysis atmospheres. Aromatic substances produced by PS, such as styrene, preferentially reduce NiO, resulting in a slightly nickel-rich alloy. This effect explains the observed peak shift and highlights the influence of the pyrolysis atmosphere on the alloy composition and lattice parameters. For the spent NCM811 and NCM622 cathodes, the leaching efficiency of Li^+ (**Fig. 5b**) is above 90% and 99.9%, respectively. **Figs. 5, c to f** are SEM images of the co-pyrolysis products of NCM811/PET/plastics after water leaching. The SEM images show that the uniformity of CNTs prepared from PC is better than those of PS, LDPE, and PP, and the CNT diameter distribution of LDPE and PP is wider. **Figs. 5, g to j** are SEM images of NCM622/PET after pyrolysis and washing with LDPE, PP, PC, and PS, respectively. The size range of the NiCo alloy was statistically analyzed semi-quantitatively (**Fig. S38**). Compared with NCM811, the nano-alloy particles of NCM622 products are more densely distributed, as shown in the bright area in SEM images. However, the length of CNTs is significantly shorter than that of products prepared from NCM811. SEM images of the products obtained by catalytic co-pyrolysis using various plastics are provided (**Figs. S39 to S46**). In addition, the carbon conversion rates of HDPE, LDPE, PP, PC, and PS can reach 33%, 29%, 23%, 36%, and 25%, respectively, among which the mass ratio of MWCNT prepared from HDPE to the catalyst (MWCNT: catalyst) is 1437 wt% (**Fig. S47**). The upcycling process of two types of spent cathode materials and five types of plastics to $(Ni_xCo_y)MnO/CNTs$ illustrates the universality of the spent NCM and binary PET-plastic co-pyrolysis process.
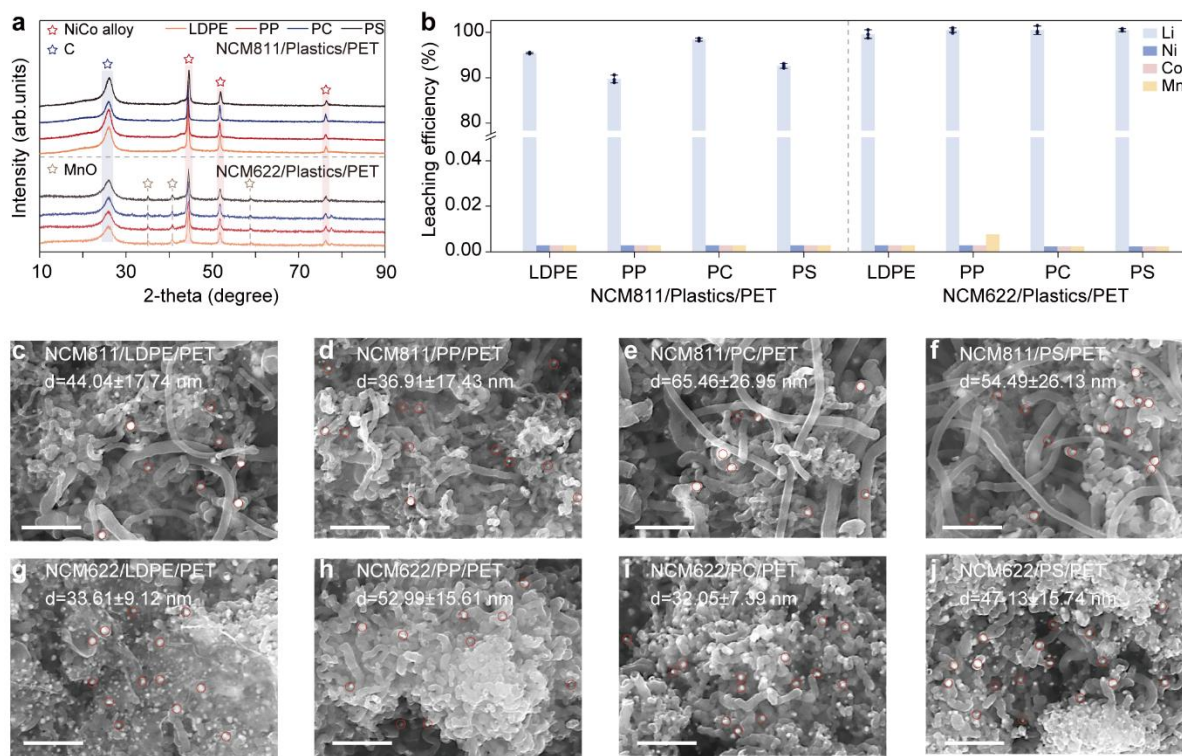
Fig. 5. Universality of $(Ni_xCo_y)MnO@CNT$ prepared by co-pyrolysis of binary plastics. Co-pyrolysis recovery conditions of plastic wastes (LDPE, PP, PC, and, PS), PET, and two spent LIB cathodes (NCM811 and NCM622) under LIB cathodes/Plastics/PET mass ratio = 1:30:1, 550 °C, 5 h. **a,** PXRD patterns, **b,** Li, Ni, Co and, Mn leaching efficiency **c-j,** SEM images, scale bar is 500 nm. Error bars indicate the standard deviation of three independent measurements. Representative SEM images are shown; the experiments were independently repeated three times with similar results.

Environmental impact characterisation was conducted using the ReCiPe 2016 Midpoint (H) v1.03 method, which is suitable for midpoint-oriented, policy-relevant evaluation of environmental burdens. Based on indicator quality, data robustness, and alignment with the study's sustainability objectives, 8 key factors were selected from 18 impact categories (**Fig. 6a**) for in-depth analysis as shown in **Tables S4-6**. These indicators provide a balanced view of climate, air, water, and resource-related impacts and were computed separately for each scenario. The resulting midpoint scores were used to rank the sustainability performance of the four recycling options. For climate change (GWP100), the upcycling route demonstrated the lowest global warming potential (0.882 kg CO_2 eq), which is only 47.5% of the emissions from the pyrometallurgical process (1.855 kg), 36.0% of Hydro (2.451 kg), and 34.5% of Direct regeneration (2.555 kg). This result highlights the strong carbon mitigation potential of upcycling, especially in alignment with carbon neutrality targets. Under the per-waste FU, Upcycling shows the lowest GWP100 (0.883 kg CO_2-eq kg^{-1}) and ranks first in 13/18 midpoints, Pyro leads in TAP, ODP∞, PMFP, HOFP and EOFP with Upcycling being second (median gap ≈14%, **Table S4**, **Table S5**).

In addition, we combined the Everbatt model of the Argonne Laboratory to conduct an environmental and economic analysis of the mixed plastic pyrolysis process. Assuming an annual processing capacity of 20000 tons of spent NCM811 cathodes at a plant in China, four different recycling methods were modeled: pyrometallurgical (Pyro), hydrometallurgical (Hydro), direct regeneration (Direct), and co-pyrolysis upcycling (Upcycling) (**Figs. S48 to S51**). Environmental analysis comparing four methods reveals the significant advantages of the upcycling process in terms of total energy consumption, water consumption, and greenhouse gas emissions (GHG, **Fig. 6b** and **Table S7**). Furthermore, the upcycling process demonstrates the highest profitability among the four recycling methods. In particular, (Ni_8Co_1)MnO/CNTs upcycled from spent NCM811 generate profits as high as $ 1497.89 per kg (**Fig. 6c**). This substantial profit potential enhances the economic competitiveness of upcycling spent NCM811 cathodes through co-pyrolysis upcycling (**Table S8**).
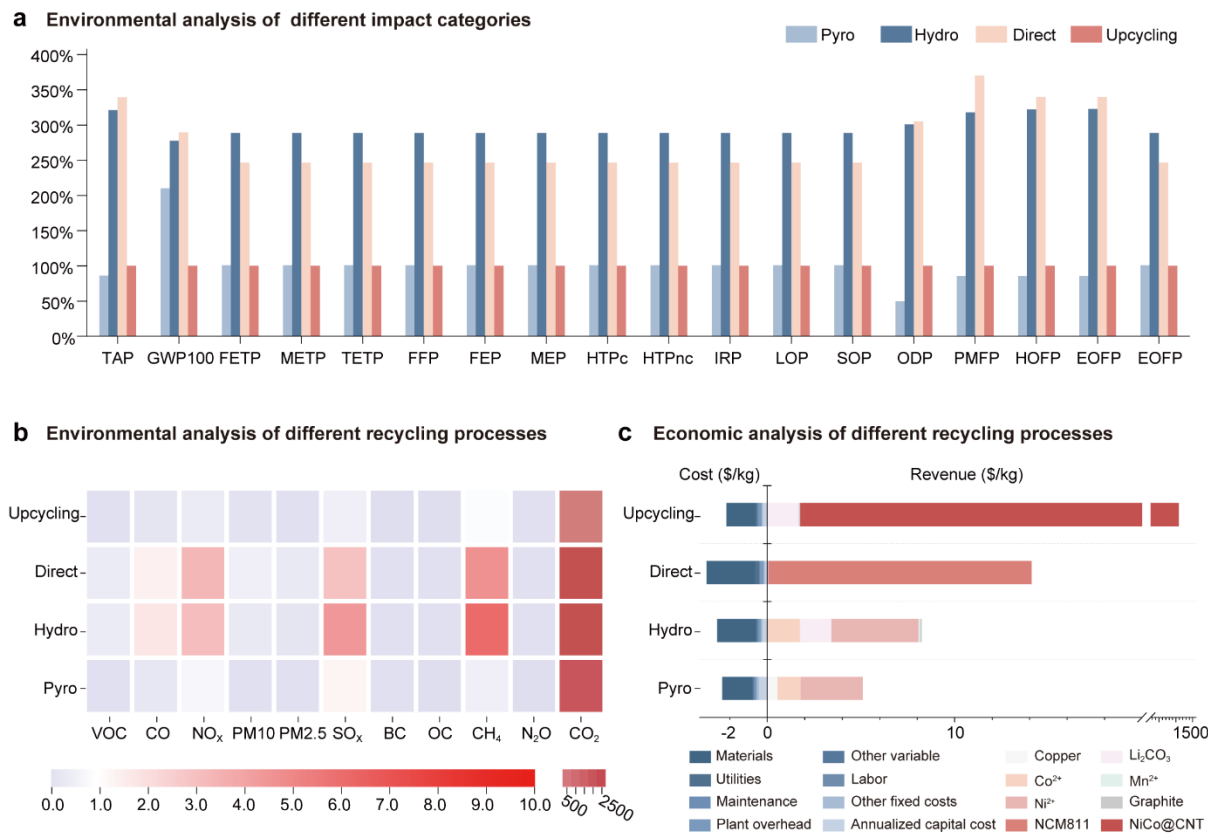
a Environmental analysis of different impact categories

Pyro | Hydro | Direct | Upcycling

b Environmental analysis of different recycling processes

c Economic analysis of different recycling processes

Fig. 6. Environmental and economic analysis of the different treatment methods for waste NCM cathodes and binary plastics *via* OpenLCA and Everbatt model. Environmental and economic analysis of pyrometallurgical (Pyro), hydrometallurgical (Hydro), direct regeneration (Direct) and co-pyrolysis upcycling (Upcycling) recycling methods **a,** The environmental impact assessment of different recycling processes of waste NCM cathodes and binary plastics *via* OpenLCA. For all the 18 impact categories, upcycling is defined as the reference for normalization **b,** Environmental analysis of the NCM811 recycling processes and **c,** the corresponding economic analysis *via* Everbatt model. The definitions of the acronyms appearing in (a) can be found in Table S5.

Discussion

The co-pyrolysis of spent NCM and PET-containing binary plastics can prepare $(Ni_xCo_y)MnO/CNT$ microwave-absorbing materials with controlled particle size and compositions. Polyethylene terephthalate (PET) prevents the deactivation of $NiCoMnO_x$, and the generated lithium carbonate (Li_2CO_3) acts as a template to control the NiCo particle size of less than 100 nm and make the NiCo active to catalyze the growth of CNTs. The process achieves the highly selective growth of CNTs at a relatively low pyrolysis temperature of 550 °C and a high carbon conversion rate of 33%. Li is recovered as Li_2CO_3 with a leaching efficiency of >98.0% without the use of mineral acids, and the toxic gases could be decomposed by the $NiCoMnO_x$ catalyst. Notably, after a simple thermal treatment, the microwave absorption performance of the material is significantly enhanced, with an effective absorption bandwidth (EAB) of 7.01 GHz at 2.41 mm. LCA results indicate that upcycling has strong carbon mitigation potential, especially in alignment with carbon neutrality targets. In summary, a co-upcycling method is achieved to prepare functional materials from spent LIBs, PET, and other plastics. This approach effectively addresses environmental challenges associated with waste plastic and spent LIBs, aiming to recover valuable metals and prepare functional catalysts. More broadly, PET-enabled co-pyrolysis is a universal and environmentally friendly solution for managing waste organics and electronic products.

Methods

Chemicals and materials. Three commercial (AR grade) LTMO cathode materials, layered oxide $LiNi_{0.8}Co_{0.1}Mn_{0.1}O_2$ (NCM811) and layered oxide $LiNi_{0.6}Co_{0.2}Mn_{0.2}O_2$ (NCM622) were purchased from Sinopharm Group Co. Ltd. Polyethylene terephthalate (PET, > 99.9 %), low-density polyethylene (LDPE, > 99.9 %), polyethylene (PE, > 99.9 %), polypropylene (PP, > 99.9 %), Polycarbonate (PC, > 99.9 %), and polystyrene (PS, > 99.9 %) were obtained from Fengtai Polymer Materials Co. Ltd. Plastic bag wastes were collected from the Northeastern University. All materials were used as received without further purification.

Recovery of spent LIB cathodes. The co-pyrolysis recovery was carried out using a 50 mL steel reactor heated in a muffle furnace (**Fig. S1**). LTMO (NCM811 and NCM622) was placed on a stainless steel, while 0.5-4 g of plastics (PE, LDPE, PP, PC, PS) were mixed with 0-0.1g of PET and placed at the bottom of the reactor. The operating temperature was maintained within a range of 400 – 550 °C (± 0.1 °C) for different durations, ranging from 10 to 300 min, with a heating rate of 5 °C·min^{-1}. Following the pyrolysis, the products on the stainless steel were transferred into a 100 mL beaker containing 80 mL of deionized water and stirred at 25 °C for 1 h. The solution was then poured into a funnel lined with a hydrophilic polyvinylidene hard pore membrane filter (d = 90 mm, pore size = 0.45 μm), and the resulting leachate was collected in a 100 mL volume flask to separate the filtrate and solid product. The filtrate was analyzed to determine the leaching efficiency of Li, Ni, Co, and Mn, while the solid product was vacuum-dried at 60 °C for 24 h. The leaching efficiency (R_i) was calculated using Eq (1):

$$R_i\ (\%)= \frac{\text{moles of recovered element i}}{\text{moles of an element in the mixed powder}} \times 100 \qquad (1)$$

To determine the contents of Li, Ni, Co, and Mn in the raw materials, the cathode materials were completely dissolved using aqua regia. Standard solutions of each element were prepared to calibrate the concentration curve. All solutions used in the experiment were prepared using deionized water, and all chemical reagents used were analytical grade.

Electromagnetic performance. The static magnetic properties of samples at room temperature

were measured by vibrating sample magnetometer (VSM, LakeShore7404) in the magnetic field range of -15 kOe to 15kOe. The samples were homogeneously mixed into a paraffin matrix and pressed to form a ring-shaped tube (inner diameter 3 mm, outer diameter 7 mm, thickness 2 mm) with a fill rate of 20 wt%, and the samples were tested by Vector Network Analyzer (VNA, Agilent PNA-E5071C) using the coaxial-line method to test the electromagnetic parameters of the samples in the frequency range of 2-18 GHz. All reported data are derived from multiple independent measurements. The electromagnetic absorption properties and loss mechanisms of the samples with 1-5 mm were obtained using the following equations:

(1) The loss angle tangent δ_ε and δ_μ are calculated from the following equations,

$$tan\delta_\varepsilon = \varepsilon''/\varepsilon' \tag{2}$$

$$tan\delta_\mu = \mu''/\mu' \tag{3}$$

where δ_ε and δ_μ are the dielectric loss angle and the magnetic loss angle, ε' and ε'' are the real and imaginary parts of the complex permittivity ($\varepsilon_r = \varepsilon' - j\varepsilon''$), and μ' and μ'' are the real and imaginary parts of the complex permeability ($\mu_r = \mu' - j\mu''$).

(2) According to Debye's theory, the relationship between the relatively complex permittivity ε_r, ε' and ε'' can be expressed by the following equations,

$$\varepsilon_r = \varepsilon_\infty + \frac{\varepsilon_s - \varepsilon_\infty}{1 - j2\pi f\tau} = \varepsilon' - j\varepsilon'' \tag{4}$$

$$\varepsilon' = \varepsilon_\infty + \frac{\varepsilon_s - \varepsilon_\infty}{1 + (2\pi f)^2\tau^2} \tag{5}$$

$$\varepsilon'' = \varepsilon''_p + \varepsilon''_c = (\varepsilon_s - \varepsilon_\infty)\frac{2\pi f\tau}{1 + (2\pi f)^2\tau^2} + \frac{\sigma}{2\pi f\varepsilon_0} \tag{6}$$

where ε_s and ε_∞ are the static dielectric constant and the dielectric constant at infinite frequency, respectively, τ is the relaxation time, and f is the frequency. ε''_p and ε''_c represent polarization loss and conductivity loss, respectively. And the relationship between ε' and ε'' can be expressed as follows,

$$\left(\varepsilon' - \frac{\varepsilon_s + \varepsilon_\infty}{2}\right)^2 + (\varepsilon'')^2 = \left(\frac{\varepsilon_s - \varepsilon_\infty}{2}\right)^2 \tag{7}$$

In the ε'-ε'' curve, each semicircle is referred to as a Cole-Cole semicircle and represents the Debye dipole polarization relaxation.

(3) The electromagnetic attenuation constant α can be calculated from the following equation,

$$\alpha = \left(\frac{\sqrt{2}\pi f}{c}\right) \times \sqrt{(\mu''\varepsilon'' - \mu'\varepsilon') + \sqrt{(\mu''\varepsilon'' - \mu'\varepsilon')^2 + (\mu''\varepsilon' + \mu'\varepsilon'')^2}} \qquad (8)$$

(4) The reflection loss (RL) is calculated according to transmission line theory, while the normalized input impedance ($Z=Z_{in}/Z_0$) is expressed as follows,

$$RL = 20 \, log \, |\frac{Z_{in}-Z_0}{Z_{in}+Z_0}| \qquad (9)$$

$$Z = \frac{Z_{in}}{Z_0} = \sqrt{\frac{\mu_r}{\varepsilon_r}} tanh[j(\frac{2\pi f d}{c})\sqrt{\varepsilon_r \mu_r}] \qquad (10)$$

where Z_{in} is the input impedance of the material, Z_0 is the free space impedance, d is the thickness of the wave-absorbing material, and c is the propagation speed of the electromagnetic wave in vacuum. In addition, the reflection loss efficiency is calculated as follows,

$$RL_{\text{Efficiency}} (\%) = 100 - (\frac{1}{10^{\frac{RL}{10}}}) \times 100 \qquad (11)$$

(5) The quarter wavelength can be calculated from the following equation,

$$t_m = \frac{n\lambda}{4} = \frac{nc}{4f_m\sqrt{|\mu_r||\varepsilon_r|}} n = (1,3,5 \dots) \qquad (12)$$

(6) RCS can be intuitively understood as a property of the target object itself, independent of the distance R. RCS is calculated from the following equation,

$$\sigma(m^2) = \lim_{R \to \infty} 4\pi R^2 (|\frac{E_S}{E_i}|)^2 = \lim_{R \to \infty} 4\pi R^2 (|\frac{H_S}{H_i}|)^2 = \lim_{R \to \infty} 4\pi R^2 \frac{S_S}{S_i} \qquad (13)$$

where E_s and E_i are the strengths of the scattered and incident electric fields, respectively; H_s and H represent the strengths of the scattered and incident magnetic fields, and S_s and S_i represent the power densities of the scattered and incident magnetic fields. In addition, since the dynamic range of radar has a very large cross-section to the target, it is usually expressed in decibel square meters (dB m^2),

$$\sigma(dBm^2) = 10log \, \sigma(m^2) \qquad (14)$$

Characterizations

The crystal phases and components of all pyrolysis products were analyzed using a Rigaku-T III X-ray diffractometer (XRD, Shimadzu X-ray 6000) equipped with Cu Kα radiation of 1.5406 Å at a scan rate of $10°·min^{-1}$ over a 2θ range from 10 to 90°. The concentrations of Li^+, Co^{2+}, Mn^{2+}, and Ni^{2+} in the solutions were determined using an atomic absorption spectrophotometer (AAS, TAS-990). Thermogravimetry-differential scanning calorimeter (TG-DSC) was used to analyze the thermal process (NETZSCH STA 449F5). Thermogravimetry-mass spectrometry (TG-MS) was performed using a thermal analyzer (Thermo plus EV2/thermo mass photo) from 30 to 600 °C at a heating rate of 10 °C min^{-1}, while N_2 gas was passed through the cavity at a flow rate of 300 mL·min^{-1}. A scanning electron microscope (SEM, FEI Quanta FEG 250) and a transmission electron microscope (TEM, JEOL Model JEM-2100F, 200 kV) were used to characterize the morphology and composition of materials. Raman spectroscopy was conducted on a Horiba Scientific HR Evolution device, utilizing an excitation wavelength of 532 nm. Fourier Transform Infrared Spectroscopy (FT-IR, Thermo Scientific Nicolet iS20) was utilized to assess the molecular and chemical composition of the samples within the wavenumber range of 400-4000 cm^{-1}. XPS was conducted on an X-ray photoelectron spectrometer (Thermo Scientific K-Alpha) and the data were analyzed using CasaXPS software. The conductivity of the samples was tested by an automated powder resistivity tester (ST2742B) using the four-probe method. The sample powder was pressed to ~1 mm thickness, and it was analyzed for warming and heat dissipation properties by an infrared thermal imaging analyzer (Testo 883), in which the warming light source was UV light with a power density of 0.57 W·cm^{-2}, the laser spot diameter was 1.3 cm, and setting time for warming up was 6 min, cooling down was 4 min.

Life cycle assessment (LCA)

We conducted a cradle-to-gate LCA in OpenLCA v1.11 in line with ISO 14040/44 to compare four spent-cathode treatment routes, i.e., pyrometallurgical (Pyro), hydrometallurgical (Hydro), direct regeneration (Direct), and co-pyrolysis Upcycling. Foreground unit processes were compiled from experimentally validated and literature-based parameters under a harmonized

accounting of energy, water, and reagents; outputs include recovered materials (e.g., Ni-Co-Mn compounds, regenerated cathodes, $NiCoMnO_x$/CNT composites) and key emissions (e.g., CO_2, NO_x, $PM_{2.5}$). Background data for electricity mixes, fuel combustion, water provision, and plastic waste recycling were sourced from Ecoinvent v3.8 (cut-off system model) with automatic provider matching and completeness/contribution checks. The functional unit (FU) used in the main text is 1 kg of spent NCM811 processed to ensure like-for-like comparison across routes; for transparency we additionally report per-product (1 kg product) results and the yield-based conversion between the two FU choices in the SI. Impact assessment followed ReCiPe 2016 Midpoint (H) v1.03; we computed the full set of 18 midpoint indicators (including GWP100, TAP, PMFP, WCP, FFP, SOP, HTP-non-carc., HOFP, and ODP∞), while highlighting eight policy-relevant ones in the main discussion. All consolidated results (per-waste and per-product), together with the route-level OpenLCA exports, are provided as SI-Data for reproducibility. Complete per-waste results are summarized in **Table S5** (18 midpoints, including ODP∞ in kg CFC-11 eq), and per-product results in **Table S4**.

Economic and environmental analysis

The EverBatt model was used to perform techno-economic and life cycle analysis of four spent battery recycling processes: pyrometallurgical (Pyro), hydrometallurgical (Hydro), direct regeneration (Direct), and co-pyrolysis upcycling (Upcycling). The EverBatt Model 2023, developed by Argonne National Laboratory, can divide the LIB closed-loop recycling process into two parts. The first part is the cost of machinery such as crushing and recycling costs, and the second part considers the cost of utilizing recycled raw materials and incorporating Li sources to achieve regeneration.

Data availability

The authors declare that the main data supporting the findings of this study are available within the article and its Supplementary Information files. Extra data are available from the corresponding author upon request. Source Data are provide with this paper.

References

1. Sagar, A.D. et al. Mission Energy Access for a just and sustainable future for all. *Nat. Energy* **8**, 1171-1173 (2023).

2. Lopez, F.A., Lauinger, D., Vuille, F. & Mueller, D.B. On the potential of vehicle-to-grid and second-life batteries to provide energy and material security. *Nat. Commun.* **15**, 4179 (2024).

3. Yang, X.-G., Liu, T. & Wang, C.-Y. Thermally modulated lithium iron phosphate batteries for mass-market electric vehicles. *Nat. Energy* **6**, 176-185 (2021).

4. Fan, E. et al. Sustainable recycling technology for Li-ion batteries and beyond: challenges and future prospects. *Chem. Rev.* **120**, 7020-7063 (2020).

5. Lee, W. et al. Advances in the cathode materials for lithium rechargeable batteries. *Angew. Chem. Int. Ed.* **59**, 2578-2605 (2020).

6. Chu, S. & Majumdar, A. Opportunities and challenges for a sustainable energy future. *Nature* **488**, 294-303 (2012).

7. Harper, G. et al. Recycling lithium-ion batteries from electric vehicles. *Nature* **575**, 75-86 (2019).

8. Ma, R. et al. Pathway decisions for reuse and recycling of retired lithium-ion batteries considering economic and environmental functions. *Nat. Commun.* **15**, 7641 (2024).

9. Ciez, R.E. & Whitacre, J.F. Examining different recycling processes for lithium-ion batteries. *Nat. Sustain.* **2**, 148-156 (2019).

10. Li, H. et al. A contact-electro-catalytic cathode recycling method for spent lithium-ion batteries. *Nat. Energy* **8**, 1137-1144 (2023).

11. Ji, G. et al. Sustainable upcycling of mixed spent cathodes to a high-voltage polyanionic cathode material. *Nat. Commun.* **15**, 4086 (2024).

12. Lou, X. et al. Grave-to-cradle photothermal upcycling of waste polyesters over spent $LiCoO_2$. *Nat. Commun.* **15**, 2730 (2024).

13. Jiao, M. et al. Recycling spent $LiNi_{1-x-y}Mn_xCo_yO_2$ cathodes to bifunctional NiMnCo catalysts for zinc-air batteries. *Proc. Natl. Acad. Sci. U.S.A.* **119**, e2202202119 (2022).

14. Liu, M. et al. Bridging li-ion batteries and fuel cells: from cathode leaching residue to an atomic-scale catalytic system. *ACS Energy Lett.* **8**, 1652-1661 (2023).

15. Li, Z. et al. Upcycling of spent $LiFePO_4$ cathodes to heterostructured electrocatalysts for stable direct seawater splitting. *Angew. Chem. Int. Ed.* **63**, e202410396 (2024).

16. Chen, M. et al. Recycling spent $LiNi_{1-x-y}Co_xMn_yO_2$ cathodes to efficient catalysts for the oxygen evolution reaction. *Green Chem.* **26**, 2912-2921 (2024).

17. Mirshokraee, S.A. et al. Upcycling of waste lithium-cobalt-oxide from spent batteries into electrocatalysts for hydrogen evolution reaction and oxygen reduction reaction: A strategy to turn the trash into treasure. *J. Power Sources* **557**, 232571 (2023).

18. Xiao, X. et al. Cathode regeneration and upcycling of spent LIBs: toward sustainability. *Energy Environ. Sci.* **16**, 2856-2868 (2023).

19. Xing, C., Yao, M. & Fei, L. Upcycling degraded layered oxide cathodes from spent lithium-ion batteries toward emerging materials: A review. *Energy Storage Mater.* **71**, 103636 (2024).

20. Zhou, F. et al. Preparation of CoO-C catalysts from spent lithium-ion batteries and waste biomass for efficient degradation of ciprofloxacin via peroxymonosulfate activation. *Chem. Eng. J.* **471**, 144469 (2023).

21. Zhu, Y., Romain, C. & Williams, C.K. Sustainable polymers from renewable resources. *Nature* **540**, 354-362 (2016).

22. Ellis, L.D. et al. Chemical and biological catalysis for plastics recycling and upcycling. *Nat. Catal.* **4**, 539-556 (2021).

23. Ma, Q. et al. Grave-to-cradle dry reforming of plastics via Joule heating. *Nat. Commun.* **15**, 8243 (2024).

24. Mentes, D. et al. Combustion behaviour of plastic waste-A case study of PP, HDPE, PET, and mixed PES-EL. *J. Clean. Prod.* **402**, 136850 (2023).

25. Sharuddin, S.D.A., Abnisa, F., Daud, W.M.A.W. & Aroua, M.K. A review on pyrolysis of plastic wastes. *Energy Convers. Manage.* **115**, 308-326 (2016).

26. Maity, A., Chaudhari, S., Titman, J.J. & Polshettiwar, V. Catalytic nanosponges of acidic aluminosilicates for plastic degradation and CO_2 to fuel conversion. *Nat. Commun.* **11** (2020).

27. Dong, Q., Lele, A.D., Zhao, X. & al., e. Depolymerization of plastics by means of electrified spatiotemporal heating. *Nature* **616**, 488–494 (2023).

28. Jiang, Y. et al. Scalable decomposition-catalysis of disposable COVID-19 face mask over self-assembly metal-doping carbocatalysts for tunable value-added products. *Appl. Catal., B.* **317**, 121735 (2022).

29. Tian, W.-W., Ren, J.-T. & Yuan, Z.-Y. In-situ cobalt-nickel alloy catalyzed nitrogen-doped carbon nanotube arrays as superior freestanding air electrodes for flexible zinc-air and aluminum-air batteries. *Appl. Catal., B.* **317**, 121764 (2022).

30. Zhou, F. et al. Balancing the components of biomass and the reactivity of pyrolysis gas: biomass-assisted recycling of spent $LiCoO_2$ batteries. *Environ. Sci. Technol.* **58**, 2102-2111 (2024).

31. Qiu, B. et al. Recycling spent Lithium-ion batteries using waste benzene-containing plastics: synergetic thermal reduction and benzene decomposition. *Environ. Sci. Technol.* **57**, 7599-7611 (2023).

32. Huang, Z. et al. Metal Reclamation from Spent Lithium-Ion Battery Cathode Materials: Directional Conversion of Metals Based on Hydrogen Reduction. *ACS Sustain Chem. Eng.* **10**, 756-765 (2022).

33. Tao, Y. et al. Carbothermal Reduction for High-Efficiency Lithium Recovery from Spent Ternary Cathode Materials. *Ind. Eng. Chem. Res.* **64**, 2531-2542 (2025).

34. Lopez-Urionabarrenechea, A., de Marco, I., Caballero, B.M., Adrados, A. & Laresgoiti, M.F. Deactivation and regeneration of ZSM-5 zeolite in catalytic pyrolysis of plastic wastes. *Waste Manage.* **31**, 1852-1858 (2011).

35. Ochoa, A. et al. Deactivation dynamics of a Ni supported catalyst during the steam reforming of volatiles from waste polyethylene pyrolysis. *Appl. Catal., B.* **209**, 554-565 (2017).

36. Chen, Z. et al. Deactivation of a Y-zeolite based catalyst with coke evolution during the catalytic pyrolysis of polyethylene for fuel oil. *Appl. Catal., A.* **609**, 117873 (2021).

37. E. Michielssen, J.-M.S., S. Ranjithan and R. Mittra Design of lightweight, broad-band microwave absorbers using genetic algorithms. *IEEE Trans. Microwave Theory Tech.* **41**, 1024-1031 (1993).

38. Hou, Y., Sheng, Z., Fu, C., Kong, J. & Zhang, X. Hygroscopic holey graphene aerogel fibers enable highly efficient moisture capture, heat allocation and microwave absorption. *Nat. Commun.* **13**, 1227 (2022).

39. Tao, J. et al. Catfish effect induced by anion sequential doping for microwave absorption. *Adv. Funct. Mater.* **33**, 2211996 (2022).

40. Qu, N. et al. 2D/2D coupled MOF/Fe composite metamaterials enable robust ultra-broadband microwave absorption. *Nat. Commun.* **15**, 5642 (2024).

41. Iqbal, A. et al. Anomalous absorption of electromagnetic waves by 2D transition metal carbonitride Ti_3CNT_x (MXene). *Science* **369**, 446-450 (2020).

42. Hui, S. et al. Highly mixed index facet engineering induces defect formation and converts the wave-transmissive mott insulator NiO into electromagnetic wave absorbent. *Adv. Mater.* **37**, e2415844 (2025).

43. Wu, L. et al. Multicolored microwave absorbers with dynamic frequency modulation. *Nano Energy* **118**, 108938 (2023).

44. Tang, Z. et al. Synthesis of $CuCo_2S_4$@expanded graphite with crystal/amorphous heterointerface and defects for electromagnetic wave absorption. *Nat. Commun.* **14**, 5951 (2023).

Acknowledgments

Competing Interest

The authors declare no competing interests.

Author Information:

Corresponding Authors

Mengjie Liu: Department of Chemistry, Northwestern University, Evanston, IL, 60202, USA; E-mail:mengjie.liu@northwestern.edu

Daxue Fu: Key Laboratory for Ecological Metallurgy of Multimetallic Mineral of Ministry of Education, School of Metallurgy, Northeastern University, Shenyang, 110819, P. R. China; E-mail: fudx@smm.neu.edu.cn

Huayi Yin: Key Laboratory for Ecological Metallurgy of Multimetallic Mineral of Ministry of Education, School of Metallurgy, Northeastern University, Shenyang, 110819, P. R. China. School of Resource and Environmental Science, Wuhan University, Wuhan, 430072, P. R. China. Key Laboratory of Data Analytics and Optimization for Smart Industry, Ministry of Education, Northeastern University, Shenyang, 110819, P. R. China; E-mail: yinhuayi@whu.edu.cn

Authors

Baolong Qiu, Yuanzhao Hou, Pin Du, Nuo Xu, Hongwei Xie, Kuiren Liu, Jianshe Chen, Binchuan Li, Qing Han: Key Laboratory for Ecological Metallurgy of Multimetallic Mineral of Ministry of Education, School of Metallurgy, Northeastern University, Shenyang, 110819, P. R. China.

Zhan Shi: Department of Land, Environment, Agriculture and Forestry, University of Padova, Legnaro (PD) 35020, Italy.

Dihua Wang: School of Resource and Environmental Science, Wuhan University, Wuhan, 430072, P. R. China.

Lawrence Yoon Suk Lee: Department of Applied Biology and Chemical Technology and the Research Institute for Smart Energy, The Hong Kong Polytechnic University, Hung Hom, Kowloon, Hong Kong SAR, P. R. China.

Author Contributions

Baolong Qiu and Yuanzhao Hou contributed equally to this work. Huayi Yin and Baolong Qiu proposed the concept, Baolong Qiu performed sample synthesis, characterization, measurement, and writing. Yuanzhao Hou performed sample characterization and electromagnetic properties analysis. Zhan Shi analysis the environmental impacts by the OpenLCA. Pin Du drew the mechanism diagram. Nuo Xu performed sample synthesis experiments. Qing Han, Hongwei Xie and Huayi Yin provided experimental conditions. Baolong Qiu and Yuanzhao Hou wrote the manuscript, Huayi Yin, Qing Han, Lawrence Yoon Suk Lee, Mengjie Liu, Kuiren Liu, Jianshe Chen, Binchuan Li and Dihua Wang revised it. All authors contributed to the entire manuscript.

Figure Legends/Captions

Fig. 1. Co-upcycling spent NCM cathodes and binary plastics. a, Conceptual design of the co-pyrolysis process of spent NCM cathodes and binary plastic wastes; **b,** Elling diagrams illustrating NCM with different pyrolysis gases; **c,** SEM images of 0 wt% PET added and 3 wt% PET added; **d,** PXRD patterns of NCM811 products; **e,** Li, Ni, Co, and, Mn leaching efficiency under different NCM811/PE/PET mass ratios (550 °C, 5 h); **f,** Regulating mechanism of PET pyrolysis gas on the growth of NiCo alloy/CNTs; **g,** Relationship between the established gas composition and temperature for the gasification of carbon. Error bars indicate the standard deviation of three independent measurements. Representative SEM images are shown; the experiments were independently repeated three times with similar results.

Fig. 2. Structural and morphological characterization of $(Ni_xCo_y)MnO/CNT$. a, PXRD patterns of $(Ni_8Co_1)MnO/CNT$-800 and $(Ni_6Co_2)MnO/CNT$-800; **b,** Raman shift of $(Ni_8Co_1)MnO/CNT$-800, $(Ni_6Co_2)MnO/CNT$-800, and, $(Ni_8Co_1)MnO/CNT$; SEM images of **c,** $(Ni_8Co_1)MnO/CNT$-800 and **f,** $(Ni_6Co_2)MnO/CNT$-800, HAADF-STEM image and the corresponding EDX mapping images of **d** and **g**; scale bar is 500 nm. High-resolution TEM image of **e** and **h**. The lattice planes of the NiCo alloy are shown

in the figure; **i,** FTIR of $(Ni_8Co_1)MnO/CNT$-800, $(Ni_6Co_2)MnO/CNT$-800, and, $(Ni_8Co_1)MnO/CNT$, **j,** C 1s spectra of $(Ni_8Co_1)MnO/CNT$-800 and $(Ni_8Co_1)MnO/CNT$; **k,** Resistivity and conductivity of $(Ni_8Co_1)MnO/CNT$-800, $(Ni_6Co_2)MnO/CNT$-800, and, $(Ni_8Co_1)MnO/CNT$. Representative SEM images are shown; the experiments were independently repeated three times with similar results.

Fig. 3. Effect of preparation conditions of $(Ni_xCo_y)MnO/CNT$ on microwave absorption performance. a, Violin plots of the real (ε', red) and imaginary (ε'', blue) parts of the complex permittivity as a function of the NCM811/PE/PET mass ratio (left) and heating temperature (right). The central line indicates the mean value, and the inner lines represent the first and third quartiles (25th and 75th percentiles). Squares connected by dashed lines show the average values. Data were obtained from n = 3 independent measurements. Complex permittivity; EMWA performance of $(Ni_8Co_1)MnO/CNT$, $(Ni_8Co_1)MnO/CNT$-800, and, (Ni_6Co_2) MnO/CNT-800, **b, c,** and **d,** 2D RL values, **e, f,** and **g,** impedance matching for |Z-1|, **h,** attenuation constant, **i,** polarization loss ε_p'' and conduction loss ε_c'' and **j,** corresponding $\varepsilon_p''/\varepsilon_c''$.

Fig. 4. Schematic diagram of electromagnetic wave absorption and heat dissipation performance of $(Ni_xCo_y)MnO/CNT$. a, Wave absorption mechanism diagram; **b,** RCS simulation curves and **c,** 3D RCS signals of PEC substrate covered with $(Ni_8Co_1)MnO/CNT$, $(Ni_6Co_2)MnO/CNT$-800, and, $(Ni_8Co_1)MnO/CNT$-800; **d,** Heating and cooling curves of $(Ni_8Co_1)MnO/CNT$-800 and **e,** corresponding digital images.

Fig. 5. Universality of $(Ni_xCo_y)MnO@CNT$ prepared by co-pyrolysis of binary plastics. Co-pyrolysis recovery conditions of plastic wastes (LDPE, PP, PC, and, PS), PET, and two spent LIB cathodes (NCM811 and NCM622) under LIB cathodes/Plastics/PET mass ratio = 1:30:1, 550 °C, 5 h. **a,** PXRD patterns, **b,** Li, Ni, Co and, Mn leaching efficiency **c-j,** SEM images, scale bar is 500 nm. Error bars indicate the standard deviation of three independent measurements. Representative SEM images are shown; the experiments were independently repeated three times with similar results.

Fig. 6. Environmental and economic analysis of the different treatment methods for waste NCM cathodes and binary plastics *via* OpenLCA and Everbatt model. Environmental and economic analysis of pyrometallurgical (Pyro), hydrometallurgical (Hydro), direct regeneration (Direct) and co-pyrolysis upcycling (Upcycling) recycling methods **a,** The environmental impact assessment of different recycling processes of waste NCM cathodes and binary plastics *via* OpenLCA. For all the 18 impact categories, upcycling is defined as the reference for normalization **b,** Environmental analysis of the NCM811 recycling processes and **c,** the corresponding economic analysis *via* Everbatt model. The definitions of the acronyms appearing in (a) can be found in Table S5.

Editorial Summary:

This study demonstrates a sustainable strategy to co-upcycle spent lithium-ion batteries and plastic waste into carbon nanotube composites with microwave absorption, enabling efficient metal recovery while reducing environmental and carbon impacts.

Peer review information: *Nature Communications* thanks Guangming Li, and the other, anonymous, reviewer(s) for their contribution to the peer review of this work. A peer review file is available.